International Journal of Solids and Structures 97–98 (2016) 200–208

Contents lists available at ScienceDirect

International Journal of Solids and Structures

journal homepage: www.elsevier.com/locate/ijsolstr

In-situ X-ray study of the deformation mechanisms of non-woven polypropylene

Naigeng Chen[a], Margaret K.A. Koker[b], Simge Uzun[c], Meredith N. Silberstein[a,*]

[a] Sibley School of Mechanical and Aerospace Engineering, Cornell University, NY14850, USA
[b] Cornell High Energy Synchrotron Source, Cornell University, NY14850, USA
[c] Department of Fiber Science and Apparel Design, Cornell University, NY14850, USA

ARTICLE INFO

Article history:
Received 7 January 2016
Revised 28 June 2016
Available online 25 July 2016

Keywords:
Computed tomography
X-Ray diffraction
Polymer fibers
Mechanical properties

ABSTRACT

Non-wovens are of emerging research and industrial importance due to the characteristic high surface area, high porosity, high damage tolerance, and low cost. However strength and toughness are difficult to design for due to the structural irregularity and multitude of deformation mechanisms. Here we investigate the mechanical properties and deformation mechanisms of polypropylene non-wovens as a function of areal weight. Mechanical characterization showed that higher areal weight corresponds to equivalent stiffness and greater strength per weight compared to lower areal weight. Two x-ray studies were carried out with synchrotron radiation during uniaxial tensile testing: micro-computed tomography (3D microstructure) and x-ray diffraction (fiber orientation). These techniques combined to reveal that in compact non-wovens inter-fiber bonds provide strong constraints on the network structure and limit fiber rotation until the bonds fail. Conversely, in sparse non-wovens localized fibers align, plastically deform, and eventually fracture. These comprehensive combined mechanical response and microstructural data sets will serve to build microstructure-based constitutive models in future work.

1. Introduction

Non-wovens are fibrous materials manufactured without a weaving or knitting process. A typical non-woven consists of a set of fibers oriented according to a manufacturing process determined statistical distribution. Due to versatile manufacturing methods, high porosity and high impact absorption capabilities, non-woven materials constitute a rapidly growing portion of the textile industry, with demonstrated applications in a variety of fields including energy, water, ballistic protection, tissue engineering and medical disposables (Ahmed et al., 2015; Huang et al., 2003; Liu et al., 2013; Russell, 2006; Yoon et al., 2008). Non-woven mechanics are complex and still poorly understood due to the random nature of fiber distributions and their evolution under straining (Picu, 2011). A better understanding of the relationship between microstructure and macroscale mechanical behavior will improve and accelerate the non-woven design process.

The relationship of non-woven elasticity to microstructure and constituent material has been established with increasing fidelity over the last 60 years. In pioneering work conducted by Cox (Cox, 2002), the elastic properties of a fiber network consisting of long, straight, non-interacting fibers were established to depend on the initial fiber orientation, fiber cross-sectional area, and intrinsic fiber elastic modulus. This framework was later extended to 3D fiber orientation distributions (Narter et al., 1999). Later studies revealed that initial fiber curvature and fiber bending can both significantly influence elastic network properties (Pai et al., 2011a; 2011b; Shahsavari and Picu, 2012; Wilhelm and Frey, 2003), decreasing stiffness and increasing in-plane Poisson's ratio. Sparse networks with high fiber length to diameter aspect ratios tend toward bending-dominated rather than stretching-dominated elasticity (Shahsavari and Picu, 2012; Wilhelm and Frey, 2003).

The relationship of non-woven mechanical properties to microstructure and constituent material under large deformation remains challenging to establish due to the combination of fiber deformation, fiber orientation, and fiber-fiber contact change. Material strength depends on both specimen size and boundary conditions with long range correlations among stresses in the fibers (Hatami-Marbini and Picu, 2009; Kulachenko and Uesaka, 2012). Prior work on thermally-bonded polypropylene non-wovens demonstrated that bond damage leads to extensive fiber realignment. The speed of the realignment process results in

* Corresponding author.
E-mail address: ms2682@cornell.edu, meredith.silberstein@gmail.com (M.N. Silberstein).

http://dx.doi.org/10.1016/j.ijsolstr.2016.07.028
0020-7683/

strain rate dependent failure modes (Jubera et al., 2014; Ridruejo et al., 2011). In order to properly describe the large transverse strain observed in high aspect ratio non-wovens in uniaxial tensile tests, fiber elastic-plastic bending needed to be considered (Silberstein et al., 2012). Bond damage is the main damage mechanism in paper-like materials (Isaksson et al., 2006; 2004). Bronkhorst (Bronkhorst, 2003) studied the elastic-plastic behavior of a 2D fiber network and found that neglecting connectivity through the thickness caused a significant disparity with experiment results.

One promising avenue to understanding non-woven mechanics is to characterize microstructure change during deformation. Micro-computed tomography (μCT) generates a 3D image of a material and has been successfully applied to a variety of non-wovens such as paper (Isaksson et al., 2012), gas diffusion layers (Tötzke et al., 2014), and needle punched (Jeon et al., 2014) and point bonded non-wovens (Demirci et al., 2011). Changes in structural parameters, including pore size, fiber orientation and contact efficiency, have been computed. X-ray diffraction (XRD) experiments on fiber networks with crystalline fibers probe for information such as orientation distribution changes. The anisotropic fiber realignment behavior of a needle punched polyethylene non-woven was revealed through XRD in a recent work by Martínez-Hergueta et al. (2015).

The aim of this paper is to elucidate the deformation mechanisms of a series polypropylene (PP) non-wovens and explore the effects of areal weight on mechanical behavior. Through the application of synchrotron radiation, non-woven microstructure changes under uniaxial tensile loading were imaged. Structural information (number of bonds, volume fraction and fiber orientation distribution) was extracted to quantitatively describe damage progression and the fiber realignment process. Specifically, μCT was used to visualize the deformed material configurations at strains spanning elastic, pre-, and post-yield regions. It was observed that low areal weight non-woven had more damage than high areal weight counterparts at same strain. Moreover, XRD experiments were used to continuously track local fiber orientation change in both monotonic tensile and stress relaxation tests. The kinematic constraints imposed by bonds were apparent through the limited fiber realignment in high areal weight non-wovens at small strains. The experimental results also indicated whether fiber bending was a significant deformation mode for each of the different areal weight non-wovens.

2. Experimental

2.1. Materials

The Dupont Typar geotextile series of non-wovens used in this investigation are composed of PP fibers with diameters ranging in size from 40 μm to 60 μm. The fibers are created by extrusion and stretched to induce a semi-crystalline structure. These fibers are randomly distributed and bonded into a sheet by applying simultaneous heat and pressure Han. The manufacturing process results in both isolated fibers and small fiber bundles within the material (Ridruejo et al., 2011). The three investigated non-wovens, SF20, SF32 and SF65, are differentiated by thickness, areal weight, and the fiber-filled volume fraction of the material (Table 1). All three quantities increase following the sequence: SF20, SF32, SF65. These materials essentially consist of layers of fibers, however most fibers do cross between layers over relatively short distances. SF20, SF32, and SF65 have approximately 7, 9, and 12 layers of fibers respectively.

Table 1
Material properties of the investigated non-wovens provided by the manufacturer Han, where $v_f = a_w/(t\rho_{fiber})$ and $\rho_{fiber} = 946$ kg/m^3.

Material Type	Thickness t (mm)	Areal weight a_w (g/m^2)	Volume fraction v_f
SF20	0.35	68	0.205
SF32	0.43	110	0.270
SF65	0.59	220	0.394

2.2. Characterization of mechanical behavior

A Zwick/Roell Z010 testing system was used to characterize the mechanical properties of the non-wovens and single PP fibers under uniaxial tension. The load was recorded using a 10 kN and a 20 N load cell for non-woven and fiber tests, respectively. Five specimens of each non-woven type were tested to capture specimen dependent variation. Rectangular non-woven specimens 45 mm in length and 9 mm in width were tested with the gauge length set to 27 mm. This gauge dimension was chosen to achieve uniaxial tension while keeping the width small enough to image with the μCT setup (explained in Section 2.3.1). A limited set of experiments were also performed on larger and smaller specimens with results provided in the supplementary materials. The thickness of each specimen was measured at three different locations with a micrometer to determine an average initial cross-sectional area. To create single fiber specimens, fibers were extracted from non-woven SF20 by tweezers and then glued on a cardboard template, spanning across a 15 mm cut-out region on the cardboard. The single fiber diameter was measured at nine locations under an optical microscope prior to testing. Force and crosshead displacement were converted to engineering stress and engineering strain by dividing by the initial cross-sectional area and the initial gauge length respectively. Specimens were elongated at a constant strain rate of 0.00588 s^{-1} until failure to determine the Young's modulus E, strength σ_f and failure strain ϵ_f. Cyclic tests were carried out at a strain rate of 0.00588 s^{-1} for loading, unloading, and reloading portions; strains at the start of the unloading steps range from 0.02 to 0.8. The unloading modulus was calculated from the first 0.02 strain of each unload. To investigate relaxation behavior, another set of specimens were stretched at a constant strain rate of 0.00588 s^{-1} to an engineering strain of 0.1 and held at constant strain for 10 min. A stretched exponential function (Williams and Watts, 1970) was fit to the normalized stress relaxation curve to obtain a characteristic relaxation time.

2.3. Synchrotron X-ray studies

X-ray studies were performed at the F3 beamline at the Cornell High Energy Synchrotron Source (CHESS). A Si(111) double crystals monochromator was used to tune the incident X-ray beam energy to 10 keV and 8 keV for the μCT and XRD experiments, respectively. The resulting energy bandwidth was on the order of 10^4. For the μCT imaging, the second Si(111) crystal was replaced with 5° miscut Si(111) crystal to increase the size of the incident beamspot on the specimen and allow for a larger imaging region. A custom-built dual actuator load frame (see supplementary material) was used at the F3 beamline for in-situ deformation throughout the X-ray experiments. The same 27 mm by 9 mm gauge section was used for all X-ray experiments as for the Zwick mechanical testing.

2.3.1. Micro-computed tomography

Changes in the 3D microstructure of the non-woven specimens, induced by deformation, were monitored using in-situ μCT imag-

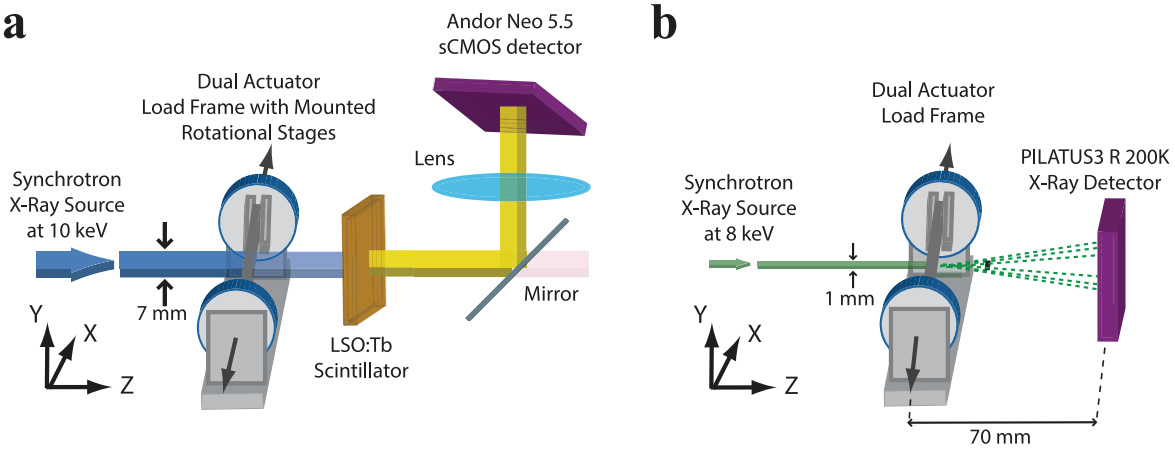

Fig. 1. (a) Schematic of in-situ μCT experimental setup. The load frame stretches the specimen to a specific strain and then rotates the specimen 180° as absorption radiographs from the incident synchrotron beam are recorded with a CMOS detector. (b) Schematic of in-situ XRD experimental setup. The load frame stretches the specimen continuously as diffraction patterns from the incident synchrotron beam are recorded on an X-ray detector.

ing. The experimental setup is shown in Fig. 1a. The X-ray beamsize was 7 mm by 7 mm. An LSO:Tb scintillator, a lens system and an Andor Neo 5.5 sCMOS detector were employed to convert the attenuated X-ray beam passing through the specimen into absorption contrast radiographs. For each tomograph (μCT scan), the specimen was rotated 180° about the loading axis in 0.25° steps (721 radiographs total). Sets of radiographs with 0.5 s exposure time were acquired. A 5 min relaxation time was added before each scan to ensure morphology change during imaging was minimal. Dark images (closed shutter) and beam profile images (open shutter, no specimen) were also acquired using the same exposure time. Elongation of the non-woven specimens was incremented in a step-wise manner to strains of 0, 0.01, 0.02, 0.1, 0.15 and 0.3. At each of the 6 strains, a scan was performed. Specimen dimensions and the methods of mechanical testing are the same as used for the mechanical behavior characterization in Section 2.2. Two specimens of each areal weight were tested during this experiment.

The raw radiographs, as well as beam profile and dark images, were processed into a stack of cross-sectional slices using the commercial software Octopus Oct. Each slice consisted of 1000 pixels by 1000 pixels with a corresponding pixel size of 6.5 μm. The commercial software AVIZO Fire AVI was used for image denoising and data visualization.

Microstructural changes were quantified in terms of changes in volume fraction v_f and bond numbers. These analyses were performed with user-written Matlab R2015a scripts Mat. In order to account for the irregular material shape at finite deformation, the reconstructed volume was divided into 20 × 20 grids on the initial specimen plane (XY plane as shown in Fig. 1). The reported v_f at each strain is the mean of v_f values calculated within each grid space. The v_f within each grid space was defined as the maximum v_f along the thickness direction with fixed sampling volume. Since the calculation of v_f is sensitive to the intensity threshold of the image stack, the threshold value was selected such that the initial calculated v_f of each specimen matches the values given in the material data sheet as provided in Table 1. Bond number is defined as the total number of connected bonding regions in the 3D image. A voxel is within a bonding region as long as its minimal distance to the background is larger than a threshold value. This bond identification approach is an upper bound estimate that utilizes the flattening caused when the non-woven is bonded with combined heat and pressure to distinguish bonds from non-bonded contacting fibers.

2.3.2. X-Ray diffraction

In-situ XRD experiments provide information about fiber orientation during deformation of the non-wovens. The experimental setup is shown in Fig. 1b. The x-ray beamsize on the specimen was 1 mm by 1 mm. Diffraction patterns were captured by a PILATUS3 R 200K detector placed 70 mm behind the specimen. Individual diffraction patterns were captured of six different single fibers extracted from the SF20 material. For the non-woven loading experiments, each specimen was either stretched to failure or to a certain strain and then allowed to relax, following the mechanical test methods described in Section 2.2. The specimens were loaded at a strain rate of 0.00588 s^{-1} corresponding to a range in strain of 0.003 per diffraction pattern. For both continuous loading and relaxation experiments, a series of XRD patterns were recorded with an exposure time of 0.5 s each.

The collected XRD patterns represent the sum of the diffraction from each of the individual fibers within the diffraction volume. The orientation distribution function is a measure of the orientation distribution of fibers in the non-woven specimen, which can be computed by resolving the intensity distribution of a diffraction ring by azimuthal angle. This diffraction pattern intensity distribution to fiber orientation distribution extraction is unique since we utilize a peak corresponding to only one orientation of the fiber. It is assumed that strain within individual fibers has negligible effect on the orientation analysis; this assumption is assessed in the supplementary material. In order to quantify the realignment process during the deformation process of non-wovens, the ensemble averaged orientation parameter p is calculated:

$$p = 2\langle \cos^2 \alpha \rangle - 1 \tag{1}$$

where α is the angle between fiber axis and loading axis. An in-plane randomly oriented set of fibers will have an orientation parameter value of 0. If all fibers are aligned perpendicular to the loading axis p is -1, and if all fibers are aligned along the loading axis p is 1. Image processing and analysis calculations were performed in Matlab R2015a Mat.

3. Results and discussion

3.1. Non-woven mechanical behaviors

The non-wovens used in this study deform elastic-plastically under uniaxial tensile loading (Fig. 2). Due to the random nature of the material, the variations in mechanical response from specimen

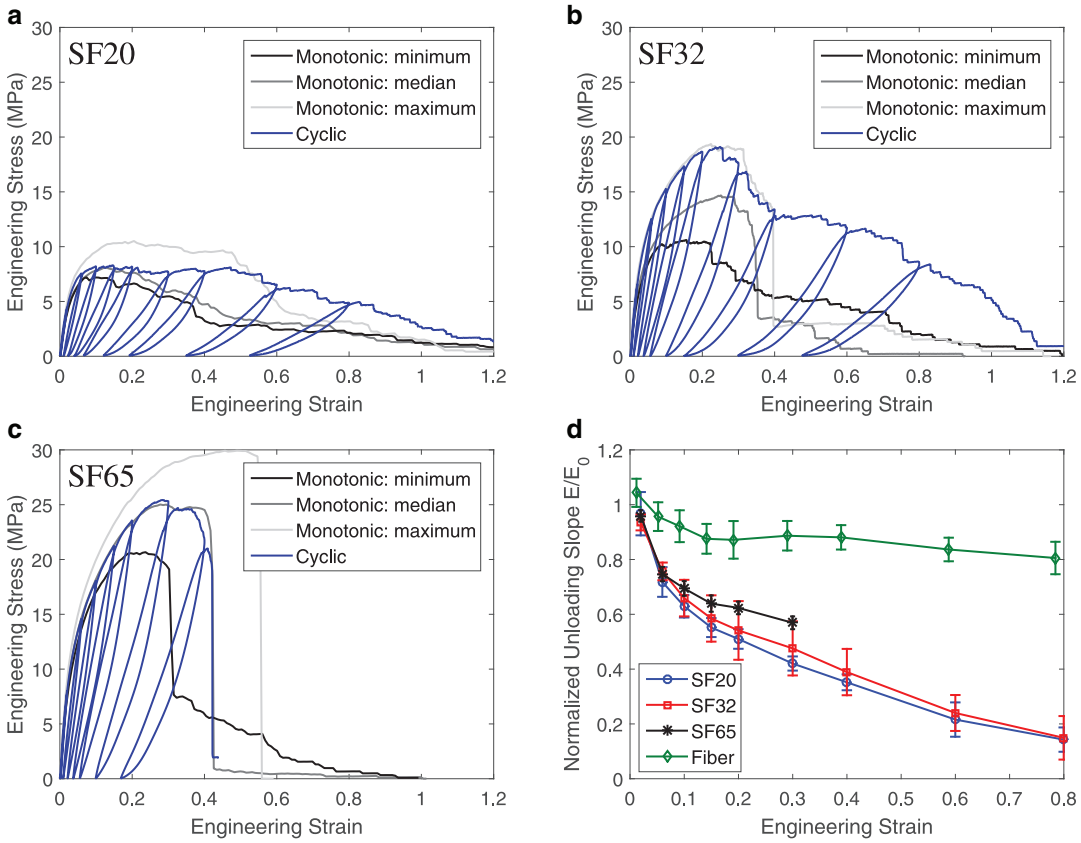

Fig. 2. Mechanical characterization of three types of non-wovens. Monotonic and cyclic uniaxial tensile behaviors of (a) SF20, (b) SF32 and (c) SF65. Due to large specimen to specimen variations, the maximum, median and minimum strength tests are shown. (d) Normalized unloading slope versus the strain when unloading step started.

Table 2
Mechanical properties of constituent fibers and non-wovens under uniaxial tensile loading. Young's modulus and strength are scaled by volume fraction v_f.

Material	Scaled modulus E/v_f (GPa)	Scaled strength σ_f/v_f (MPa)	Failure ϵ_f	Relaxation time τ (10^4 s)
Fiber	2.45 ± 0.15	293 ± 8	1.3 ± 0.3	1.9 ± 0.3
SF20	0.78 ± 0.03	31 ± 3	0.15 ± 0.06	1.39 ± 0.18
SF32	0.84 ± 0.07	42 ± 7	0.21 ± 0.06	1.66 ± 0.15
SF65	0.85 ± 0.04	52 ± 5	0.33 ± 0.08	1.83 ± 0.10

to specimen are large. Three representative monotonic curves are included in Fig. 2, corresponding to three tests of maximum tensile strength, median tensile strength and minimum tensile strength. The stress-strain curve of each areal weight has similar shape before the peak stress, consisting of a short linear region followed by a gradual roll over region. All of the curves are smooth at the beginning and become jagged starting around the peak stress, by which point fiber breakage is visually apparent. The three different areal weight materials are qualitatively distinct in the post-peak stress failure evolution. The failure of SF20 (lowest areal weight) progresses gradually, resulting in a long tail on the stress-strain curve. Some SF32 (intermediate areal weight) specimens undergo gradual failure, while others have sharp decreases in stress after the peak stress. All SF65 (highest areal weight) specimens have rupture-like failure. It is important to note that these specimens exhibit a more gradual damage mode than would be seen at larger specimen sizes (see supporting material). The differences in mechanical properties among the three areal weights are summarized in Table 2. Material of higher areal weight has higher stiffness, higher strength, later failure initiation and longer relaxation time. When the mechanical response is scaled by volume fraction, the three non-wovens have similar scaled Young's moduli, but the scaled strength of the more compact non-wovens is higher. This means that on a per weight basis the more compact material has better strength without compromising stiffness.

Material damage can be evaluated macroscopically with cyclic loading. In Fig. 2a-c, representative cyclic stress-strain curves of three types of non-wovens are overlaid on the uniaxial tensile curves. A permanent set (non-zero strain at zero stress) is present after each unloading step for all three areal weights. This permanent set comes from a combination of fiber plastic deformation and material structure damage (Ridruejo et al., 2012). Damage also manifests as a decreased unloading slope with deformation. The differences in the degradation process among the three types of non-wovens are evident in Fig. 2d, in which unloading slopes are normalized by the initial Young's moduli and plotted against the strains when unloading initiated. All the non-woven normalized moduli decrease once the macroscopic deformation was imposed. At each strain, normalized unloading modulus increases with increasing areal weight (SF20, SF32 and SF65).

For the three non-wovens made from the same constituent fiber and made through the same manufacturing process, high

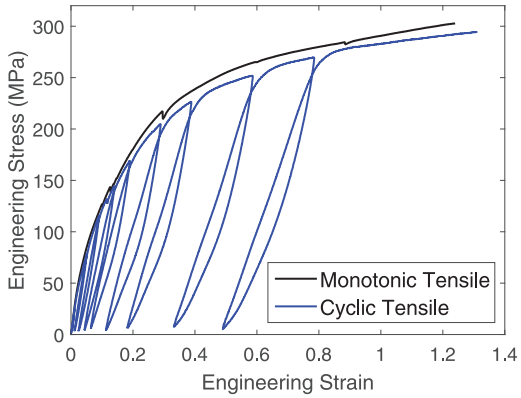

Fig. 3. Tensile stress-strain characterizations of single PP fibers.

areal weight non-wovens are stiffer, stronger, less stretchy and less degraded before the large scale failure than low areal weight non-wovens. In order to better understand these observations from mechanical tests, detailed characterizations of constituent fibers and microstructure deformation were carried out and are discussed in the following sections.

3.2. Fiber mechanical behaviors

The constituent fibers are elastic-visco-plastic, as is typical for thermoplastic polymers. In Fig. 3, the tensile stress-strain curves exhibit a linear region followed by gradual yield and then linear hardening. The fracture is rupture-like, occurring around a strain of 1.3. In the cyclic tests, large hysteresis loops and permanent sets are observed after the unloading step, even when the fibers are stretched to small strains. The mechanical properties of fibers are listed in Table 2. The fiber modulus is approximately three times the scaled non-woven Young's moduli, which is consistent with theoretical predictions for non-bonded long fiber networks (Cox, 2002). This indicates that initial non-woven elasticity is at most minimally related to bond properties. The similarity of non-woven and fiber relaxation constants suggests that non-woven relaxation is due to individual fiber relaxation.

3.3. Non-woven 3D microstructure in tension

Non-woven deformation involves a combination of fiber deformation, relative fiber movement and bond damage. The 3D microstructures of an SF32 specimen at four different strain states are shown in Fig. 4. Prior to deformation, the material was predominantly planar with thickness variation on the order of the fiber diameter. Fibers were randomly oriented in the specimen (XY) plane, with corresponding non-uniform pore sizes and distributions. Interweaving is apparent among the fibers. Fibers are distorted from their cylindrical shape in contact regions between the fibers. The fibers were observed to be long with little curvature. Dangling fiber ends were not apparent except at the edges of the material. At a strain of 0.02, minimal change in material microstructure could be seen. As the specimen was stretched to a strain of 0.1, a combination of both straight and wavy fibers were observed, with the later aligning mostly along the direction transverse to the applied tension. Some fibers bent out of the material plane forming an arc-shape structure. Overall, the material surface was no longer planar. At a strain of 0.3, consolidation of fibers across the transverse direction occurred, and the specimen edges became jagged. The majority of the fibers that remained straight were well aligned with the loading direction. Due to large scale damage, fibers separated into layers in the through thickness direction, resulting in a loosely connected network.

A comparison of the microstructures of the three non-woven types at a strain of 0.1 is shown in Fig. 5. Of the three non-wovens, the width reduction of the SF20 specimen was the most significant. Fibers aligned with the transverse direction were mostly sinuous, which was evident in the loosely connected regions compressed by the surrounding highly bonded regions. In some parts of the (comparatively thin) SF20 specimen, the whole material became wavy and delamination occurred on the specimen scale. In contrast, the high areal weight non-woven, SF65, remained mostly planar at this same strain. The arced fiber segment lengths were short. Unlike the low areal weight counterparts, no large bulges formed by bundles of bending fibers were observed in SF65. The multiple layers of the non-woven help to stabilize each other and provide increased strength relative to a material consisting of independent layers.

The number of bonded regions and filled volume fraction are used here to quantitatively describe structural damage in non-wovens (Fig. 6). Number of bonds is a crucial characteristic, since bonds hold the fibers together and provide strength to the material. SF65 had more than double the initial bonds of SF32 and more than four times that of SF20. The number of bonds in all three non-wovens decreased starting from a strain of 0.02 indicating the bond fracture initiated at small strains. Until a strain of 0.15, the bond number drop in SF20 was almost the same as SF65. Considering the fraction of initial bonds, the relative bond fracture in SF20 was more significant. The SF32 specimen shown here

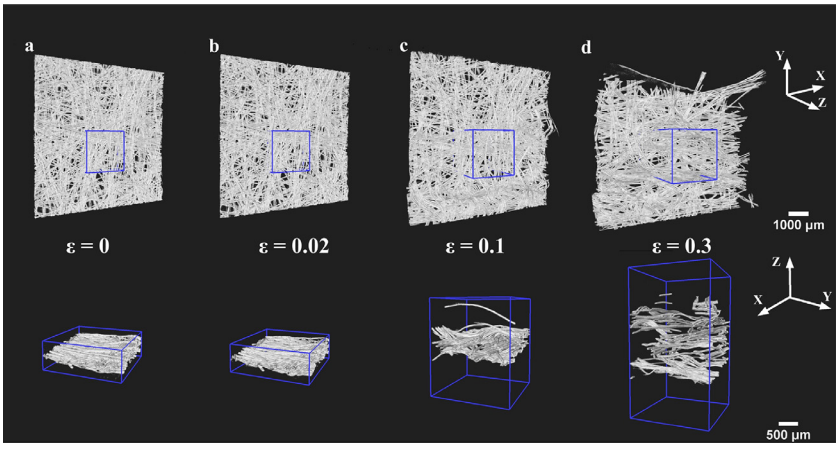

Fig. 4. 3D microstructure images of a non-woven SF32 specimen at strains of (a) 0, (b) 0.02, (c) 0.1 and (d) 0.3. Top: full 6.5 mm by 6.5 mm reconstructed volume. Bottom: an enlarged partial view.

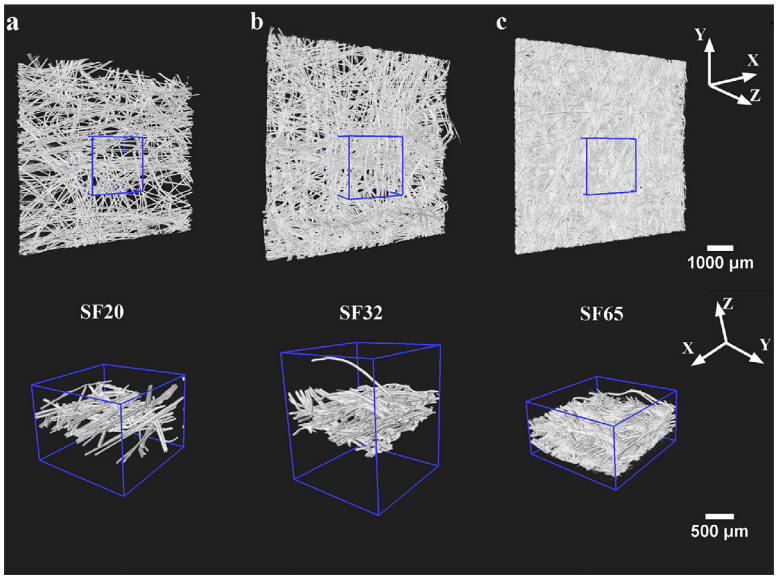

Fig. 5. 3D microstructure images of non-woven specimens (a) SF20, (b) SF32 and (c) SF65 at a strain of 0.1. Top: full 6.5 mm by 6.5 mm reconstructed volume. Bottom: an enlarged partial view.

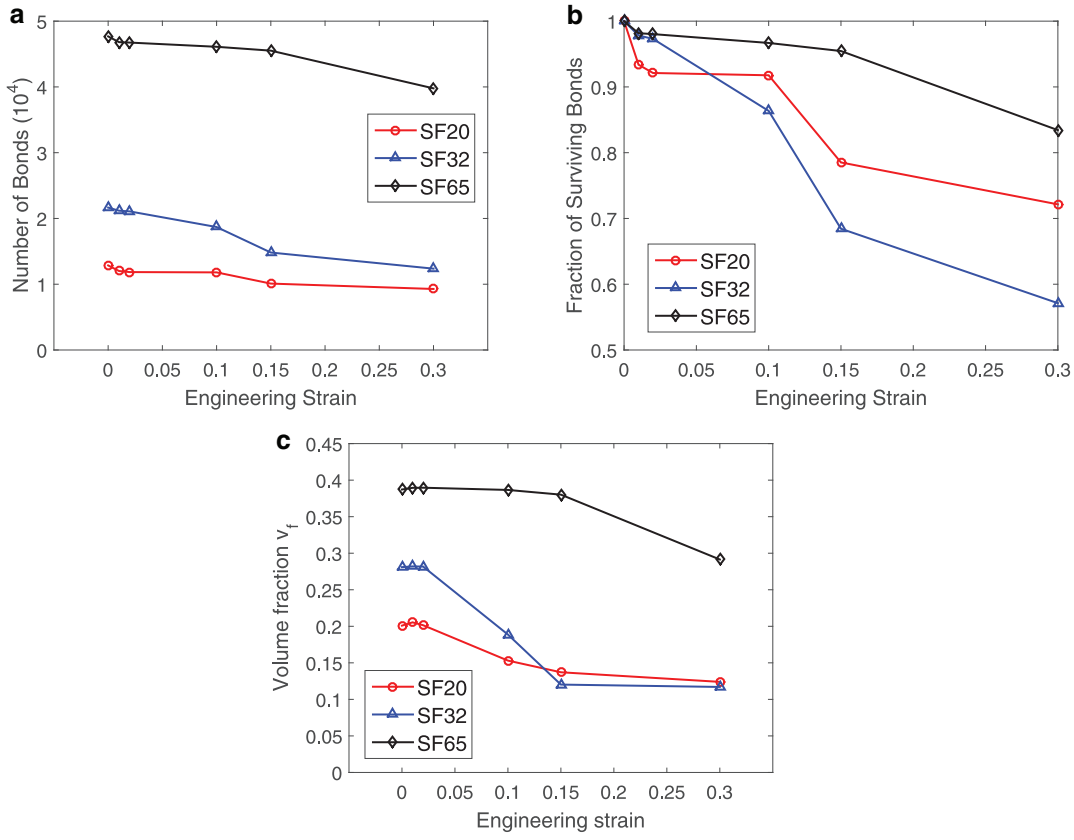

Fig. 6. The evolution of (a) number of bonds, (b) fraction of initial bonds that remain and (c) volume fraction v_f as a function of applied strain.

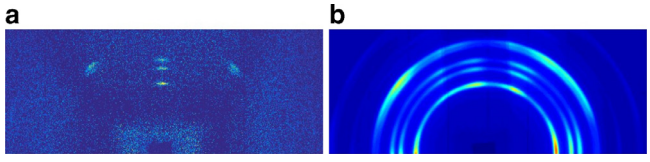

Fig. 7. 2D XRD pattern of (a) a single PP fiber and (b) an undeformed SF32 non-woven specimen.

has more bond fracture than SF20. Looking into the corresponding stress-strain curve (see supplementary material), it was found that this SF32 specimen is severely damaged before a strain of 0.1. In larger samples since the number of fibers engaged in supporting the load increases with increasing specimen size as the influence from artificially short fiber segments near the edge is reduced; this may result in either greater or lesser bond survival depending on the bond strength distribution. At the onset of large scale damage,

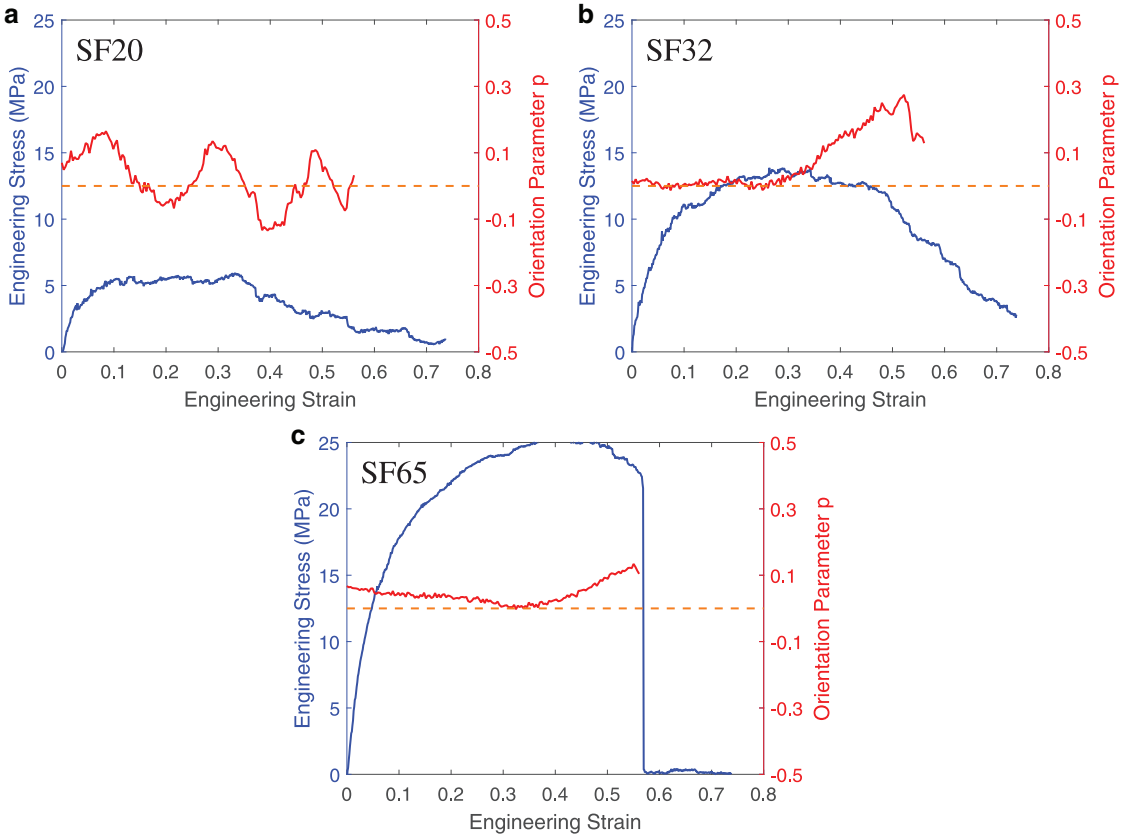

Fig. 8. Stress and orientation parameter as a function of strain for (a) SF20, (b) SF32 and (c) SF65.

bonds over a relatively localized strip of the material are responsible for the ultimate failure of the non-woven, so the total bond count does not decrease as drastically as might otherwise be expected. Decreases in volume fraction, a result of material delamination, are indicative of interlayer bond fraction and fiber out of plane bending that locally increases the specimen thickness more than the width contracts from fiber alignment. The volume fraction of SF20 and SF32 were relatively constant until a strain of 0.02 and then decreased significantly, while the volume fraction of SF65 remained relatively constant until the scan at a strain of 0.15. The observations of decreasing number of bonds and decreasing volume fraction show that structural damage in the low areal weight non-woven initiated at smaller strains. Also, structural damage is more drastic for low areal weight material than for high areal weight ones. These conclusions support the analysis of material degradation in cyclic test section for which unloading slope decreased more drastically for the low areal weight non-woven than for the high areal weight non-woven.

3.4. Fiber orientation evolution under loading

Fiber orientation distribution is a key factor in determining non-woven behaviors. In non-wovens composed of ductile fibers, the degree of fiber alignment due to tensile loading is significant at finite strains (Silberstein et al., 2012; Yano et al., 2012). Fiber alignment determines how the force supported by each fiber adds up to the overall non-woven stress and is indicative of whether the non-woven accomodates deformation by fiber stretching (high energy) or fiber bending and rotation (low energy). XRD experiments were carried out in order to study the areal weight effects on the fiber alignment.

The PP fibers present in the non-wovens are semicrystalline with axisymmetric crystalline orientation, which makes XRD a feasible method for probing fiber orientation distribution. Fig. 7a shows the XRD pattern of a single horizontally aligned fiber (parallel to the loading axis). Three diffraction peaks are observed at an azimuthal angle of 90°, and two others peak can be seen at azimuthal angles of 50° and 130°. The 2θ angles of these peaks are 14.2°, 17.1°, 18.7° and 22.1° corresponding to crystalline planes aligned in (110), (040), (130), and (111) and (131) directions, respectively. This diffraction pattern is consistent with alpha phase PP fibers (Iijima and Strobl, 2000). Each individual fiber has the same diffraction pattern. Therefore, a one-to-one relationship between fiber orientation and diffraction spot (2θ and azimuthal angle) location can be used to track fiber orientation in the non-woven. The intensity distribution along the azimuthal angle of a ring represents fiber angular distribution. The average diffraction pattern of an undeformed SF32 specimen is shown in Fig. 7b.

The fiber orientation evolution in the non-wovens during uniaxial tensile loading is shown in Fig. 8. Detailed orientation distribution functions can be found in the supplementary material. Here, homogenized orientation parameter p (Eq. 1) is plotted as a function of applied strain. Changes in p may differ somewhat with specimen size, particularly for SF20. The differences in the orientation evolution process among the three materials are readily apparent. The orientation parameters of SF32 and SF65 were nearly constant until a strain of 0.3 and 0.4 respectively, at which point each increased monotonically until large scale failure. The onset of realignment in both materials occurred just prior to the peak stress and the orientation parameter is much less than predicted with an affine deformation assumption (see supplementary material). On

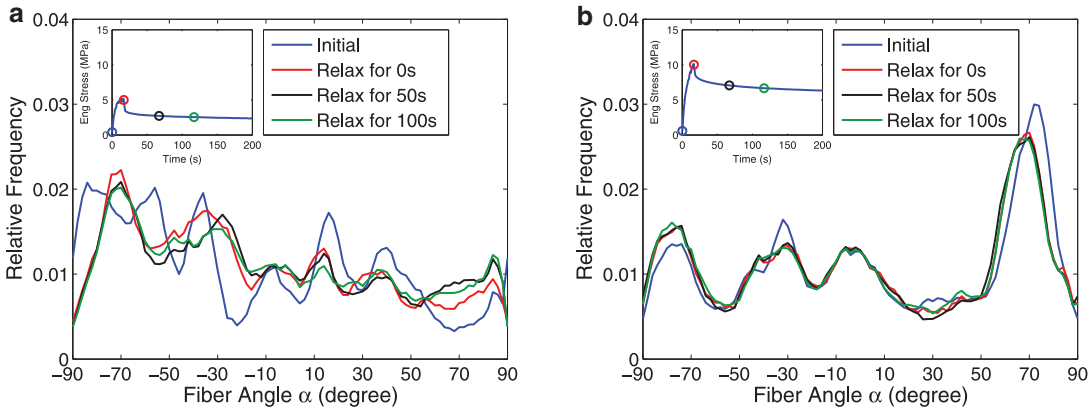

Fig. 9. Fiber orientation change at four time points for (a) SF20 and (b) SF32. Inset: stress relaxation curve. The SF65 specimen (not shown) behaved similarly to the SF32.

the contrary, the orientation parameter of SF20 increased from the beginning until a strain of 0.1, and then fluctuated with no overall trend. In high areal weight non-wovens, the discrepancy between the timing of fiber reorientation and the initiation of deformation can be explained by two reasons. First, the existence of large number of bonds provides strong constraints and limits the fiber-fiber rotation. Second, due to short bond-to-bond segment lengths, fibers are more difficult to bend, and hence the fibers transverse to the loading direction kinematically inhibit rotation of partially aligned fibers with the loading direction. SF20 is a sparse network and has long fiber segment length between bonds. Bond damage quickly affects the fiber orientation with fibers tending to bend and rotate, so that fiber realignment starts at small strains. Since the incident XRD beam is only 1 mm by 1 mm, the exact values of these orientation parameters vary from specimen to specimen, particularly at strains larger than the peak stress for which strain inhomogeneity is significant, however these trends hold across specimens.

Even though fiber alignment was observed in all three types of non-wovens, the unloading slope decreases in the cyclic tests. This decrease demonstrates that the effect of fiber alignment is overcome by bond damage and fiber fracture. One should also note that bond fracture changes the network topology, leading to a structure in which fibers are longer and easier to bend. The orientation parameters of high areal weight non-wovens therefore change sharply (Fig. 8) at finite strains when bond fracture reaches a great extent.

The constraints provided by bonds are also evident in the stress relaxation tests. In Fig. 9, two representative sets of fiber orientation curves taken during relaxation tests are shown. Each plot consists of four curves corresponding to fiber orientation distributions at four different time points: the initial point, the start point of relaxation, 50 s and 100 s after relaxation. For the SF32 specimen (and the not shown SF65), there was minimal fiber orientation change within 100 s of relaxation time. For the SF20 specimen, the number of fibers aligned in -30° and 70° changed significantly during the first 50 s of relaxation. This orientation change stems from fiber reorientation due to bond breakage as was evident in the surface images taken by an optical camera. Bond breakage during relaxation was only observed in specimens that were already largely damaged prior to relaxation. This indicates that as long as the strong bond constraints remain, the non-woven microstructure is “frozen” during the relaxation period, and the macroscopic stress relaxation mainly originates from fiber relaxation rather than structure change.

4. Conclusion

In this work, the deformation mechanisms of a series of thermally-bonded PP non-wovens and the dependence of these mechanisms on areal weight were investigated. Mechanical characterization revealed the elastic-plastic behavior of the material, as well as two distinct areal weight dependent failure modes: gradual damage progression and rupture-like failure. Higher areal weight non-wovens tended to fail in a rupture-like manner, whereas lower areal weight material failed gradually. Moreover, higher areal weight non-wovens exhibited higher mass scaled strength, larger failure strain and longer relaxation time. Mechanical characterization of the constituent PP fiber revealed that the fiber is also elastic-plastic with stiffness close to three times the scaled non-woven stiffness, suggesting bond properties do not affect initial non-woven elasticity. The deformation process of three types of non-wovens were visualized by in-situ μCT experiments. As applied macroscopic strain increased, fiber bending and internal fiber layer delamination became visually apparent. In higher areal weight material, the bending segment length was shorter and width reduction was less compared to lower areal weight material at the same strain. The volume fraction and bond number decrease in the highest areal weight material (SF65) are less significant than the other two materials at low strains. At strains past the peak stress all the non-wovens exhibit a decrease in tangent stiffness and number of bonds. In-situ XRD experiments were used to track non-woven fiber orientation evolution during tensile loading and relaxation. The initiation of significant fiber realignment in high areal weight material was observed in the middle of the rollover yield region, which can be explained by the large bond number density and short bond-to-bond fiber segment length. In contrast, large scale damage occurred much earlier in the low areal weight non-woven (SF20) resulting in an irregular fiber orientation evolution process. Localized sets of fibers aligned, plastically deformed, and eventually fractured. In the stress relaxation experiments, stress decreased in all cases. Fiber orientation only occurred if large scale damage was present prior to the start of the strain hold period.

This study reveals the transition of non-woven microstructure from predominantly planar to 3D under tensile loading. The structural reorganizations observed here indicate that considering interweaving and the fiber-fiber connectivity in the thickness direction is necessary for predicting non-woven mechanical strength. Moreover, the strong influence of bond damage on the fiber realignment process points to the need to accurately capture bond properties. Each of these observations will be applied in future work.

Acknowledgment

We appreciate the technical support from CHESS staff scientists. Special thanks to Ernest Fontes for his support throughout the project, Sean Quanckenbush for initial design and construction of the dual actuator load frame, Robin Baur for guidance on CT reconstruction, and Rong Huang and Darren Dale for experimental hardware setup. This work is based upon research conducted at the CHESS which is supported by the National Science Foundation and the National Institutes of Health/National Institute of General Medical Sciences under NSF award DMR-1332208. The authors also thank Kintex Industries, LLC for providing material.

Supplementary material

Supplementary material associated with this article can be found, in the online version, at 10.1016/j.ijsolstr.2016.07.028.

References

Ahmed, F.E., Lalia, B.S., Hashaikeh, R., 2015. A review on electrospinning for membrane fabrication: Challenges and applications. Desalination 356, 15–30. doi:10.1016/j.desal.2014.09.033. URL http://linkinghub.elsevier.com/retrieve/pii/S0011916414005190.

Avizo, Fire 8.1. URL http://www.fei.com/software/avizo3d/.

Bronkhorst, C., 2003. Modelling paper as a two-dimensional elasticplastic stochastic network. doi:10.1016/S0020-7683(03)00281-6.

Octopus, 8.7. URL https://octopusimaging.eu/octopus/octopus-reconstruction.

Cox, H.L., 2002. The elasticity and strength of paper and other fibrous materials. Br. J. Appl. Phys. 3 (3), 72–79. doi:10.1088/0508-3443/3/3/302.

Demirci, E., Acar, M., Pourdeyhimi, B., Silberschmidt, V.V., 2011. Finite element modelling of thermally bonded bicomponent fibre nonwovens: Tensile behaviour. Comput. Mater. Sci. 50 (4), 1286–1291. doi:10.1016/j.commatsci.2010.02.039. URL http://linkinghub.elsevier.com/retrieve/pii/S0927025610001072.

Dupont Typar, Geosynthetics Handbook, Technical Report.

Hatami-Marbini, H., Picu, R.C., 2009. Heterogeneous long-range correlated deformation of semiflexible random fiber networks. Phys. Rev. E - Stat., Nonlinear, Soft Matter Phys. 80 (4), 1–11. doi:10.1103/PhysRevE.80.046703.

Huang, Z.M., Zhang, Y.Z., Kotaki, M., Ramakrishna, S., 2003. A review on polymer nanofibers by electrospinning and their applications in nanocomposites. Comp. Sci Technol. 63 (15), 2223–2253. doi:10.1016/S0266-3538(03)00178-7.

Iijima, M., Strobl, G., 2000. Isothermal crystallization and melting of isotactic polypropylene analyzed by time-and temperature-dependent small-angle X-ray scattering experiments. Macromolecules 5204–5214. URL http://pubs.acs.org/doi/abs/10.1021/ma000019m.

Isaksson, P., Dumont, P.J.J., Rolland Du Roscoat, S., 2012. Crack growth in planar elastic fiber materials. Int. J. Solids Struct. 49 (13), 1900–1907. doi:10.1016/j.ijsolstr.2012.03.037.

Isaksson, P., Gradin, P.a., Kulachenko, a., 2006. The onset and progression of damage in isotropic paper sheets. Int. J. Solids Struct. 43 (3–4), 713–726. doi:10.1016/j.ijsolstr.2005.04.035.

Isaksson, P., Hägglund, R., Gradin, P., 2004. Continuum damage mechanics applied to paper. Int. J. Solids Struct. 41 (16–17), 4731–4755. doi:10.1016/j.ijsolstr.2004.02.043.

Jeon, S.-Y., Na, W.-J., Choi, Y.-O., Lee, M.-G., Kim, H.-E., Yu, W.-R., 2014. In situ monitoring of structural changes in nonwoven mats under tensile loading using X-ray computer tomography. Composites Part A 63, 1–9. doi:10.1016/j.compositesa.2014.03.019. URL http://linkinghub.elsevier.com/retrieve/pii/S1359835X14000980.

Jubera, R., Ridruejo, A., González, C., LLorca, J., 2014. Mechanical behavior and deformation micromechanisms of polypropylene nonwoven fabrics as a function of temperature and strain rate. Mech. Mater. 74, 14–25. doi:10.1016/j.mechmat.2014.03.007. URL http://linkinghub.elsevier.com/retrieve/pii/S0167663614000507.

Kulachenko, A., Uesaka, T., 2012. Direct simulations of fiber network deformation and failure. Mech. Mater. 51, 1–14. doi:10.1016/j.mechmat.2012.03.010.

Liu, D.S., Ashcraft, J.N., Mannarino, M.M., Silberstein, M.N., Argun, A.a., Rutledge, G.C., Boyce, M.C., Hammond, P.T., 2013. Spray layer-by-layer electrospun composite proton exchange membranes. Adv. Funct. Mater. 23 (24), 3087–3095. doi:10.1002/adfm.201202892.

Martínez-Hergueta, F., Ridruejo, a., González, C., LLorca, J., 2015. Deformation and energy dissipation mechanisms of needle-punched nonwoven fabrics: A multiscale experimental analysis. Int. J. Solids Struct. 65, 120–131. doi:10.1016/j.ijsolstr.2015.03.018. URL http://linkinghub.elsevier.com/retrieve/pii/S002076831500133X.

Matlab, R2015a. URL http://www.mathworks.com/products/matlab/.

Narter, M.A., Batra, S.K., Buchanan, D.R., 1999. Micromechanics of three-dimensional fibrewebs: constitutive equations. Proceedings of the Royal Society A: Math., Phys. Eng. Sci. 455 (1989), 3543–3563. doi:10.1098/rspa.1999.0465.

Pai, C.L., Boyce, M.C., Rutledge, G.C., 2011. Mechanical properties of individual electrospun PA 6(3)T fibers and their variation with fiber diameter. Polymer 52 (10), 2295–2301. doi:10.1016/j.polymer.2011.03.041.

Pai, C.L., Boyce, M.C., Rutledge, G.C., 2011. On the importance of fiber curvature to the elastic moduli of electrospun nonwoven fiber meshes. Polymer 52 (26), 6126–6133. doi:10.1016/j.polymer.2011.10.055.

Picu, R.C., 2011. Mechanics of random fiber networksa review. Soft Matter 7 (15), 6768. doi:10.1039/c1sm05022b.

Ridruejo, A., González, C., Llorca, J., 2011. Micromechanisms of deformation and fracture of polypropylene nonwoven fabrics. Int. J. Solids. Struct. 48 (1), 153–162. doi:10.1016/j.ijsolstr.2010.09.013. URL http://linkinghub.elsevier.com/retrieve/pii/S0020768310003331.

Ridruejo, A., González, C., Llorca, J., 2012. A constitutive model for the in-plane mechanical behavior of nonwoven fabrics. Int. J. Solids. Struct. 49 (17), 2215–2229.

Russell, S., 2006. Handbook of nonwovens. Woodhead Publishing.

Shahsavari, A., Picu, R.C., 2012. Model selection for athermal cross-linked fiber networks. Phys. Rev. E - Stat., Nonlinear, Soft Matter Phys. 86 (1), 1–5. doi:10.1103/PhysRevE.86.011923.

Silberstein, M.N., Pai, C.L., Rutledge, G.C., Boyce, M.C., 2012. Elasticplastic behavior of non-woven fibrous mats. J. Mech. Phys. Solids 60 (2), 295–318. doi:10.1016/j.jmps.2011.10.007. URL http://linkinghub.elsevier.com/retrieve/pii/S0022509611002006.

Tötzke, C., Gaiselmann, G., Osenberg, M., Bohner, J., Arlt, T., Markötter, H., Hilger, a., Wieder, F., Kupsch, a., Müller, B., Hentschel, M., Banhart, J., Schmidt, V., Lehnert, W., Manke, I., 2014. Three-dimensional study of compressed gas diffusion layers using synchrotron X-ray imaging. J. Power Sources 253, 123–131. doi:10.1016/j.jpowsour.2013.12.062. URL http://linkinghub.elsevier.com/retrieve/pii/S0378775313020405.

Wilhelm, J., Frey, E., 2003. Elasticity of stiff polymer networks.. Phys. rev. lett. 91 (10), 108103. doi:10.1103/PhysRevLett.91.108103.

Williams, G., Watts, D.C., 1970. Non-symmetrical dielectric relaxation behaviour arising from a simple empirical decay function. Trans. Faraday Soc. 66 (1), 80. doi:10.1039/tf9706600080.

Yano, T., Higaki, Y., Tao, D., Murakami, D., Kobayashi, M., Ohta, N., Koike, J.-i., Horigome, M., Masunaga, H., Ogawa, H., Ikemoto, Y., Moriwaki, T., Takahara, A., 2012. Orientation of poly(vinyl alcohol) nanofiber and crystallites in non-woven electrospun nanofiber mats under uniaxial stretching. Polymer 53 (21), 4702–4708. doi:10.1016/j.polymer.2012.07.067. URL http://linkinghub.elsevier.com/retrieve/pii/S0032386112006611.

Yoon, K., Hsiao, B.S., Chu, B., 2008. Functional nanofibers for environmental applications. J. Mater. Chem. 18 (44), 5326. doi:10.1039/b804128h.